ARTICLE

Transparent Clay–Polymer Nano Brick Wall Assemblies with Tailorable Oxygen Barrier

Morgan A. Priolo, Daniel Gamboa, and Jaime C. Grunlan*

Department of Mechanical Engineering, Texas A&M University, 3123 TAMU, College Station, Texas 77843

ABSTRACT Thin films of sodium montmorillonite clay and branched polyethylenimine (PEI) are deposited on various substrates using layer-by-layer assembly. Films with 40 polymer–clay layers contain more than 84 wt% clay, have hardness as high as 1 GPa, and are completely transparent. Oxygen transmission rates (OTR) through these films decrease as the pH of PEI increases. These pH-tailorable properties are the result of changing PEI charge density, which causes the polymer to deposit more thickly at high pH because of low charge density. After 70 PEI (at pH 10)–clay layers are deposited onto 179 μm poly(ethylene terephthalate) film, the resulting 231 nm assembly has an OTR below the detection limit of commercial instrumentation (<0.005 cc/(m^2 day atm)). When multiplied by thickness, the resulting oxygen permeability is found to be less than 0.002 $\times$ 10^{-6} cc/(m day atm)), which is lower than values typically reported for SiOx. This is the lowest permeability ever reported for a polymer–clay composite and is believed to be due to a brick wall nanostructure created by the alternate adsorption of polymeric mortar and highly oriented, exfoliated clay platelets. Because of their high level of transparency and gas barrier, these films are good candidates for a variety of flexible electronics, food, and pharmaceutical packaging.

KEYWORDS: layer-by-layer assembly • transmission electron microscopy • thin films • oxygen barrier • clays • composites

INTRODUCTION

Layer-by-layer (LbL) assembly is a method of building multifunctional thin films through alternating exposure of a substrate to aqueous cationic and anionic mixtures (1–3), as shown schematically in Figure 1. LbL assemblies can exhibit a wide array of properties, including electrical conductivity (4–7), sensing (8–10), superhydrophobicity (11–13), antimicrobial (14–16), drug delivery (17, 18), and controlled molecule release (19). The thickness of these films is dependent upon the adsorption thickness of each layer deposited, which can be tailored by altering molecular weight (20, 21), temperature (22, 23), pH (22, 24), counterion (25), and ionic strength (26) of the deposition mixture and relative humidity of the fabrication environment (27). Each complementary pair of cationic and anionic layers is known as a bilayer and is typically 1–100 nm thick. In many cases, one or more of the deposition ingredients are charged nanoparticles. Quantum dots (28, 29), clay (30–33), silica nanoparticles (34), and carbon nanotubes (7) have been deposited in LbL assemblies to impart optoelectronic behavior, strength, antireflectivity, and electrical conductivity, respectively. In addition to exhibiting the strength of steel (35), clay-containing assemblies have been shown to have oxygen barrier properties that rival ceramic or metal thin films (36).

Transparent and flexible gas barrier films are a key component for flexible electronics (38) and pharmaceutical (39) and food packaging (40). Films exhibiting the lowest gas transmission rates typically contain inorganic oxide layers (e.g., SiO_x or Al_2O_3) (41–44), which are prone to cracking when flexed (45). The addition of clay to polymer films is an effective means to improve barrier (46–48), but these composites typically suffer from poor optical clarity and low barrier relative to oxides. Layer-by-layer assembly of polymer and clay generates thin films with comparable barrier to metal oxides and the mechanical robustness of a polymer composite (36). The brick wall nanostructure of these films, depicted in Figure 1b, effectively eliminates the issue of cracking. Meanwhile, the relative ease of production, using aqueous mixtures under ambient conditions, is another key advantage of this technique.

In the present work, growth of assemblies made with cationic polyethylenimine (PEI) and anionic montmorillonite clay are studied. Growth is shown to be strongly influenced by the pH of the PEI deposition solution. Increasing the thickness of PEI layers, by increasing pH, is shown to reduce oxygen transmission rate (OTR) by a factor of 20 and elastic modulus of these films by a factor of 2. Both of these properties are strongly influenced by the spacing between highly oriented clay layers, with thicker polymer deposition resulting in reduced OTR and modulus. With the appropriate deposition conditions, films with an OTR below 0.005 cc/(m^2 · day · atm)) (more than 3 orders of magnitude lower than the PET substrate used for deposition) or an elastic modulus above 30 GPa were produced. The former may be useful for a variety of packaging applications (flexible electronics, microwaveable food, etc.), whereas the latter is interesting for hard-coating of scratch-sensitive surfaces.

EXPERIMENTAL SECTION

Materials. Southern Clay Products, Inc. (Gonzales, TX) supplied the natural sodium montmorillonite (MMT) (trade name Cloisite Na$^+$) clay used in this study. MMT has a cationic

* Corresponding author. E-mail: jgrunlan@tamu.edu.
Received for review November 24, 2009 and accepted December 8, 2009
DOI: 10.1021/am900820k

Published on Web 12/21/2009

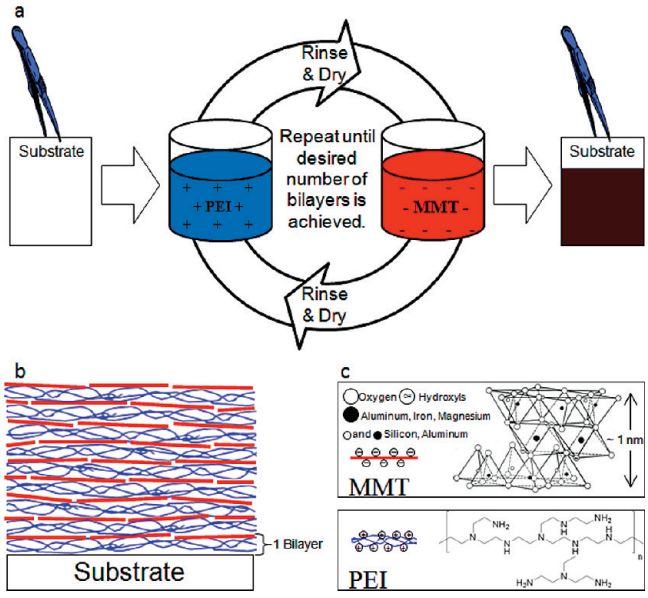

FIGURE 1. (a) Schematic of layer-by-layer assembly of polyethylenimine and clay, with (b) a cross-sectional illustration of the resulting brick wall nanostructure, and (c) a structural representation of an MMT platelet from ref (37). and PEI.

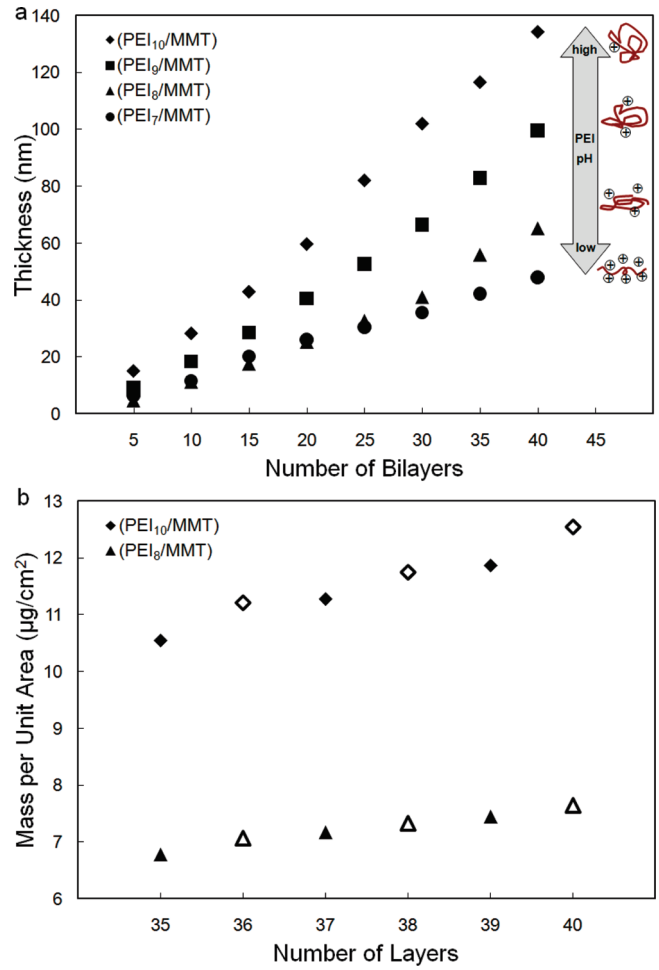

FIGURE 2. (a) Thickness as a function of bilayers deposited and (b) mass as a function of individual layers deposited for films made with clay and polyethylenimine. Thickness measurements were made with an ellipsometer using silicon wafer substrates. Mass measurements were obtained with a quartz crystal microbalance. Filled data points in b denote polymer layers, and unfilled data points denote clay layers.

exchange capacity of 0.926 meq/g and a negative surface charge in deionized water (49). Individual platelets have a reported density of 2.86 g/cm^3, diameter range of 10−1000 nm (most have $d \geq 200$ nm) and thickness of 1 nm (50). Branched polyetheylenimine (PEI) ($M_w = 25\,000$ g/mol and $M_n = 10\,000$ g/mol) was purchased from Aldrich (Milwaukee, WI). Poly(ethylene terephthalate) (PET) film with a thickness of 179 μm (trade name ST505, produced by Dupont-Teijin) was purchased from Tekra (New Berlin, WI) and used as the substrate for OTR testing. This PET film has an OTR of approximately 8.6 cc/(m^2 · day · atm) under dry conditions. Polystyrene (PS) film, with a thickness of 250 μm, was purchased from Goodfellow (Huntington, England) and used as the substrate for transmission electron microscopy. Single-side-polished (100) silicon wafers (University Wafer, South Boston, MA), 500 μm in thickness, and fused quartz glass slides (Structure Probe Inc., West Chester, PA) were used as substrates for film growth characterized by ellipsometry and UV−vis, respectively. Silicon wafers were also used as the substrate for atomic force microscopy and nanoindentation measurements. Polished Ti/Au crystals with a resonance frequency of 5 MHz were purchased from Maxtek, Inc. (Cypress, CA) and used as deposition substrates for quartz crystal microbalance characterization.

Film Preparation. The following aqueous mixtures were prepared using 18.2 MΩ deionized water from a Direct-Q 5 Ultrapure Water System (Millipore, Billerica, MA). Aqueous solutions of PEI (0.1 wt % in deionized water) were prepared by rolling for 24 h. Prior to deposition, each PEI solution's pH was altered using 1 M HCl. Anionic suspensions of MMT (0.2 wt. % in deionized water) were prepared by rolling for 24 h. For deposition onto PET or PS, substrates were rinsed with deionized water, methanol, and again with water before finally being dried with filtered air. These substrates were then corona treated using a BD-20C Corona Treater (Electro-Technic Products, Inc., Chicago), creating a negative surface charge (51, 52). For deposition onto silicon wafers and fused quartz slides, a 30-min piranha treatment was performed (53). ***Caution!*** *Piranha solution reacts violently with organic materials and should be handled with extreme caution.* These substrates were then rinsed with deionized water, acetone, and again with water before finally being dried with filtered air. Each treated substrate was then dipped in the PEI solution for 5 min, rinsed with deionized water, and dried. This procedure was followed by an identical dipping, rinsing, and drying procedure in the clay suspension. After this initial bilayer was deposited, the same procedure was followed with only 1 min dip times for subsequent layers. This procedure was repeated until the desired number of bilayers was achieved. All thin films analyzed for their barrier properties were prepared using a home-built robotic dipping system (54).

Film Characterization. Film thickness was measured using a PHE-101 Discrete Wavelength Ellipsometer (Microphotonics, Allentown, PA) at a wavelength of 632.8 nm and a 65° incidence angle. Mass increase as a function of individual layers deposited was measured using a Research Quartz Crystal Microbalance (QCM) (Maxtek Inc., Cypress, CA). Film absorbance was monitored at wavelengths between 190 and 900 nm using a USB2000-UV−vis Spectrometer (Ocean Optics, Dunedin, FL). In an effort to eliminate substrate influence on the data, thickness, mass, and absorbance measurements began after at least 5 bilayers of deposition. Thin film cross sections were imaged using a JEOL 1200EX TEM (Parbody, MA). Modulus and hardness of these assemblies were measured by Hysitron, Inc. (Minneapolis, MN) using a Hysitron TI-700 UBI nanomechanical test instrument and Diamond Cube-Corner Probe. Thin film topography was analyzed using a NanoSurf2 Atomic Force Microscope (AFM) (Nanoscience Instruments, Phoenix, AZ). AFM images were obtained in phase contrast mode with a free

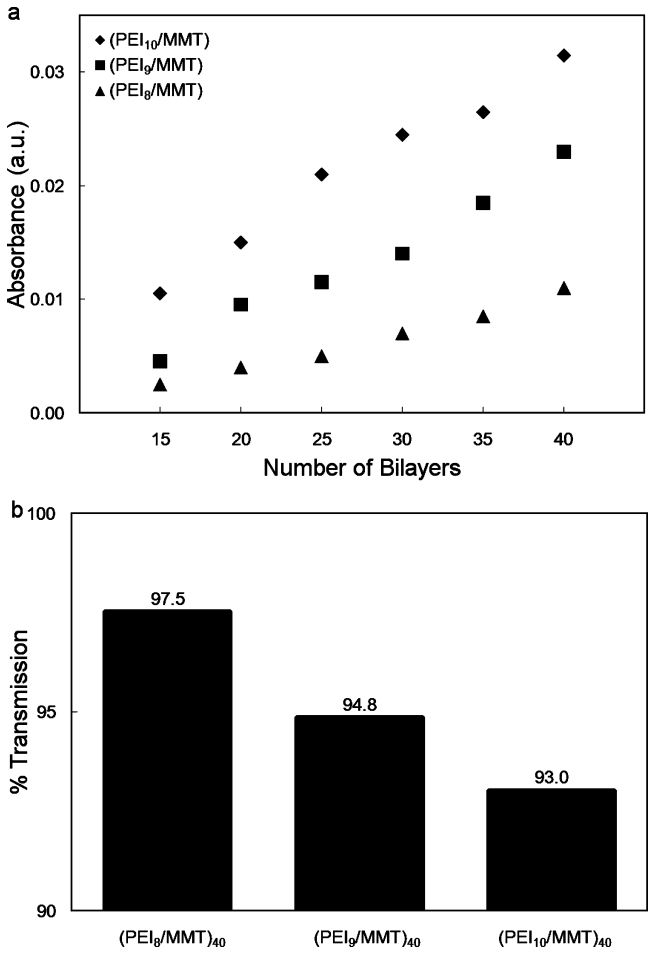

FIGURE 3. (a) Absorbance at 565 nm as a function of bilayers deposited and (b) percent transmission as a function of polyethylenimine pH for 40-bilayer films made with clay and PEI.

vibration amplitude of 100 mV using an n-type silicon cantilever with a tip radius of curvature less than 10 nm and resonance frequency of approximately 300 kHz from Vista Probes (Phoenix, AZ). OTR testing was performed by MOCON (Minneapolis, MN) in accordance with ASTM D-3985 (55), using an Oxtran 2/21 ML instrument. OTR testing was done at 23 °C and 0% RH.

RESULTS AND DISCUSSION

Influence of pH on Film Growth. As previously mentioned, the alteration of a deposition solution's pH value can change the rate of growth of an LbL film due to changes in charge density (22–24). In this case, the pH of an aqueous solution containing 0.1 wt % PEI was altered from its natural value of approximately 10.4 using 1 M HCl. Films were deposited by alternately exposing a substrate to this PEI solution and an aqueous suspension containing 0.2 wt % MMT, which was not altered from its natural pH of approximately 10. LbL films in the current study are denoted $(PEI_x/MMT)_y$, where x represents the pH of the PEI deposition solution and y represents the number of bilayers deposited. Figure 2 shows the linear growth, and the influence of PEI pH on thickness, exhibited by the combination of MMT and PEI. Films made with PEI pH 10 and pH 7 grow at a rate of 3.5 nm per bilayer and 1.2 nm per bilayer, respectively.

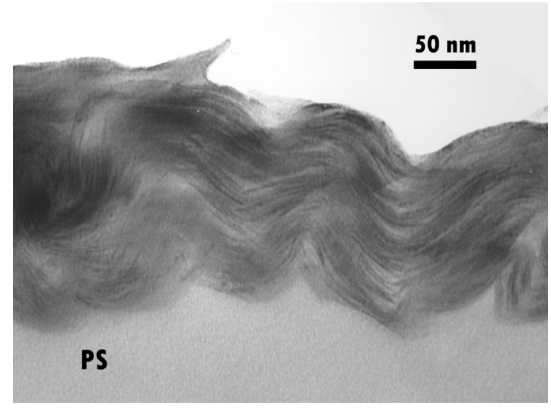

FIGURE 4. TEM cross-sectional image of a 40-bilayer film with clay and pH 10 PEI. This film was deposited on polystyrene, cured in epoxy prior to sectioning, and floated on ethylene glycol to prevent swelling.

These data show that the film growth is reduced by decreasing the pH of the PEI solution. This is due to the high charge density of PEI at low pH (56), which causes the polymer backbone to repel itself into a flattened (more straightened) state, as illustrated in Figure 2a. The opposite is true at high pH, where a lower charge density and more coiled polymer result in thicker deposition. Deposited mass per layer was measured with a quartz crystal microbalance, as shown in Figure 2b. Although the QCM data confirm the linear growth observed with the ellipsometer (Figure 2a), it also reveals the weight fraction of clay and allows the density of each nanocomposite thin film to be calculated. As expected, the thinner film, (PEI_8/MMT) has greater clay concentration (84.3 wt %) and density (2.5 g/cm^3) than its thicker (PEI_{10}/MMT) counterpart, with 76.6 wt % clay and a density of 2.27 g/cm^3. This level of clay in a bulk polymer composite is unprecedented, especially in light of the fact that these films are completely transparent, but similar to LbL assemblies with clay reported by others (35).

Visible light absorbance as a function of bilayers deposited (Figure 3a) further confirms linear growth and also highlights the optical clarity of these films. Percent transmission as a function of PEI pH of 40-bilayer films (Figure 3b) shows that optical transparency is modestly influenced by pH. In a conventional clay-filled polymer composite, a clay concentration of 20 wt % yields a transmission level of 79% at best, but in many cases these composites are much more opaque at clay concentrations below 10 wt % due to poor exfoliation (40). The $(PEI_8/MMT)_{40}$ assembly shows that optical transmission greater than 97.5% is achievable with 84.3 wt % clay. Diminishing transmission with increasing pH is minimal (less than a 5% decrease, Figure 3b) because of the increased spacing between clay layers at high PEI pH.

A TEM image of a $(PEI_{10}/MMT)_{40}$ film cross-section is shown in Figure 4. Individual clay platelets can be seen as dark lines in this film, which reveals the brick wall nanostructure shown schematically in Figure 1. This image emphasizes the high level of clay orientation, with all platelets lying parallel to the polystyrene substrate. Closer inspection of the image confirms that the majority of clay platelets deposit as single sheets, as well as the number of

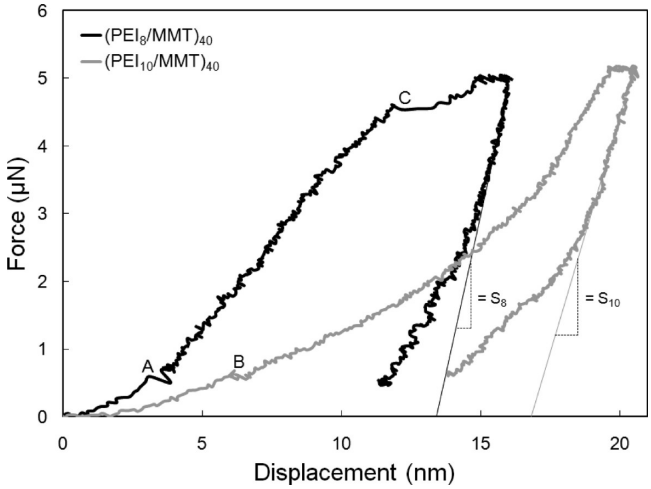

FIGURE 5. Representative force versus displacement curves of 40-bilayer thin films made of clay and PEI (pH 8 and 10) on silicon. Stiffness (*S*) is denoted by the slopes of the tangents of the unloading region, as denoted by S_8 and S_{10}.

bilayers deposited, as there are approximately 40 "rows" of clay platelets. The image also visually reveals the level of exfoliation (or separation) of clay platelets in these thin films. It is possible that the thin polymer deposition between clay layers may be considered an expanded state of intercalation (rather than true exfoliation). The thickness of this film appears greater than the ellipsometric measurements suggest (Figure 2a) because cross-sections are cut at an angle rather than perpendicularly through the film surface. The waviness of this film is likely an artifact of the TEM sample preparation, which facilitates some stress relief in films. This level of organization and structure of clay has also been observed by others and confirmed with small-angle X-ray diffraction (57). Wide-angle X-ray diffraction was performed on films deposited on silicon wafers in the present work (see the Supporting Information), which suggests increased spacing with increased PEI pH, but is not very definitive because of the relatively small number of layers. With this degree of control over the growth of these LbL films, mechanical properties, such as modulus and hardness, can also be tailored by adjusting the pH of PEI.

Thin Film Modulus and Hardness. Free-standing, clay-filled layer-by-layer thin films have been shown to have an elastic modulus as high as 125 GPa (35). The films in this study are much too thin to test as free-standing composites, so nanoindentation was used to measure modulus and hardness of 40-bilayer films. Indentation measurements were made on PEI-MMT films deposited on to silicon wafers. The force of the indenter probe was limited to approximately 5 μN to avoid substrate influence from indenting too deeply. After the linearly increased force reached its maximum, it was held constant for two seconds before being decreased (or unloaded) at a linear rate. The hardness (*H*) and elastic modulus (E_s) of the assemblies were obtained from the loading and unloading curves, such as those shown in Figure 5. Points A–C in the curves show areas of possible platelet breakage, as a minor decrease in (or constant) force can be seen coupled with a sharp increase in depth before the

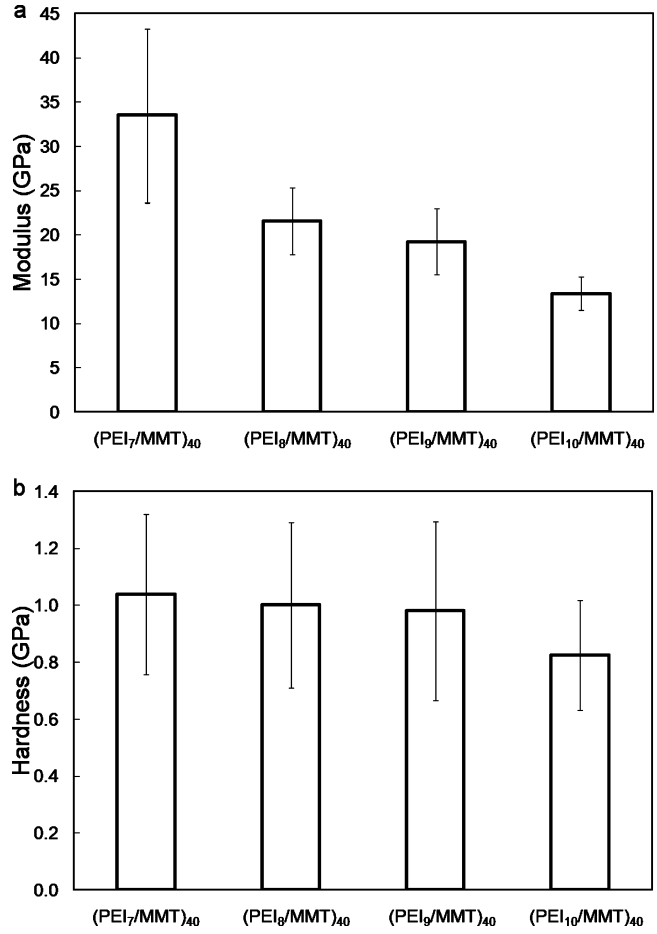

FIGURE 6. (a) Elastic modulus and (b) hardness of 40-bilayer films made with clay and PEI (at a pH of 7, 8, 9, and 10). These mechanical properties were obtained using nanoindentation.

indenter encounters the next clay layer. Thin film elastic modulus (E_s) is calculated using (58):

$$\frac{1}{E_r} = \frac{1 - \nu_i^2}{E_i} + \frac{1 - \nu_s^2}{E_s} \quad (1)$$

where ν is Poisson's ratio (s refers to the sample, and i refers to the indenter probe) and the elastic modulus of the indenter probe (E_i) is 1140 GPa. Reduced elastic modulus (E_r) is calculated using the stiffness (*S*) and the contact area (*A*) made by the tip on the sample:

$$E_r = \frac{S\sqrt{\pi}}{2\sqrt{A}} \quad (2)$$

where stiffness is taken from unloading curves (such as Figure 5) to be the initial slope of force as a function of displacement (dF/dh) multiplied by the maximum displacement (h_{max}). With a small disparity in Poisson's ratio ($\nu_i = 0.07$ and $0 < \nu_s < 0.5$ for most materials), and large difference in elastic modulus between indenter and sample, the difference between E_r and modulus of elasticity (E_s) is less than 8 GPa. Figure 6a shows that thinner films have a higher elastic modulus, up to 33.5 GPa, as expected due to greater constraint of low modulus PEI.

Hardness (*H*) is taken as the maximum force (F_{max}) divided by the contact area (*A*) made by the tip on the

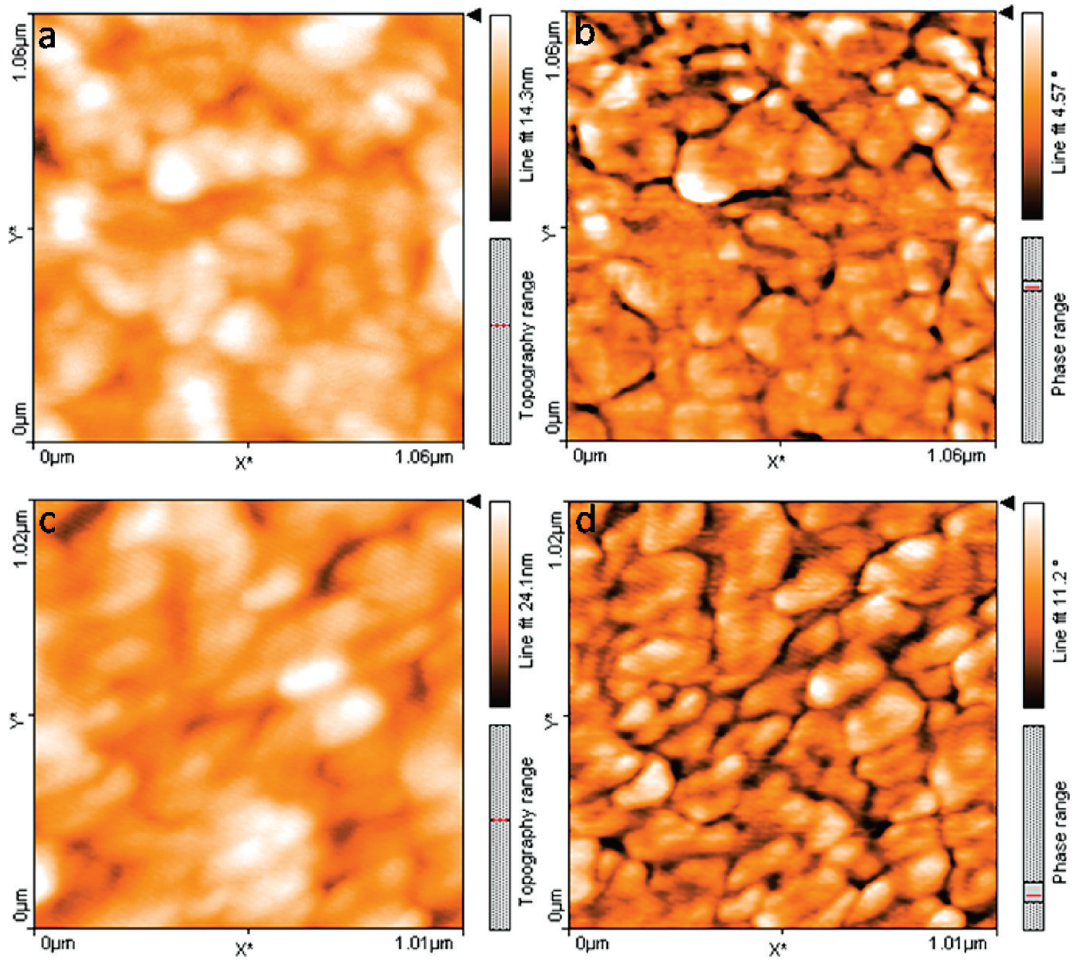

FIGURE 7. AFM height and phase images of the surface of 10-bilayer films with clay and PEI at a pH of (a, b) 8 and (c, d) 10.

sample. Maximum force is calculated using the stiffness (S) and displacement (h_{max}) of the indentation tip:

$$F_{max} = \frac{S(h_{max} - h_c)}{\varepsilon} \quad (3)$$

where h_c is contact depth, and ε is an indenter dependent geometric constant (0.75 in this case). Figure 6b shows that the hardness of these samples is nearly identical (approximately 1 GPa, within experimental error) which can be explained by the films having similar amounts and two-dimensional organization of clay. In other words, clay is deposited densely and uniformly over the surface of the film, regardless of pH, and only deposits one platelet thick. These hardness values (>0.5 GPa) are similar to those found by others for similar polymer−clay assemblies containing 100 bilayers (57). This hardness level is quite significant, especially when compared to other LbL composites created for their ultrahardness (59), and could be useful as hard-coatings.

AFM surface images shown in Figure 7 confirm the 2D organizational similarity among these assemblies and also show that surface roughness increases with pH. Height images show $(PEI_8/MMT)_{10}$ on silicon (Figure 7a) has an rms surface roughness of approximately 2.1 nm, while the $(PEI_{10}/MMT)_{10}$ film (Figure 7c) has a roughness of approximately 3.6 nm. These roughness values are further evidence of a well-aligned nanostructure (Figure 1), where the vast majority of clay deposits as sheets oriented parallel to the substrate. Moreover, the phase images (Figure 7b, d) also reveal a dense, cobblestone path structure for the clay platelets, which (combined with ideal orientation) produces gas barrier behavior. The oxygen permeability of these films is even more pH-sensitive than mechanical properties, producing low transmission rates at high pH.

Oxygen Permeability. The addition of clay to a polymer is one of the most common methods to lower its oxygen transmission rate (36, 46–48, 60, 61). The unique advantage that layer-by-layer thin film assemblies have over conventional polymer composites is the high level of exfoliation and orientation of the deposited clay platelets. With each platelet's largest dimension parallel to the substrate, or perpendicular to the diffusion direction, the effective aspect ratio is maximized. The aspect ratio for the natural sodium montmorillonite used here is more than 200 (50). This maximized aspect ratio is only realized in polymer nanocomposites with highly exfoliated clay platelets, which results in a longer diffusion length (i.e., tortuous path) and decreased permeability. A high degree of spacing between clay platelets and the preferred parallel conformation is remarkably visible in the $(PEI_{10}/MMT)_{40}$ film shown in Figure 4.

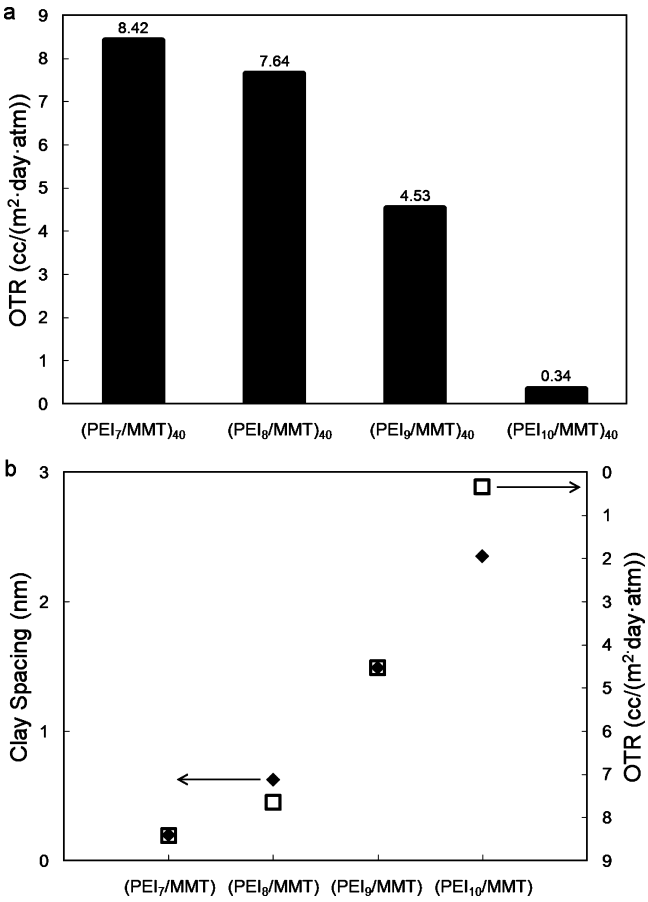

FIGURE 8. (a) Oxygen transmission rates of 40-bilayer films as a function of their PEI pH values and (b) clay spacing as a function of PEI pH with OTR of 40-bilayer films.

Montmorillonite clay can be regarded as impermeable and can dramatically decrease the oxygen transmission rate of either the polymer matrix it resides in, or the substrate on which the polymer nanocomposite film is deposited. The 179 μm thick poly(ethylene terephthalate) film, used as the substrate for gas barrier measurements, has an oxygen transmission rate of approximately 8.6 cc/(m^2 · day · atm). Figure 8a shows the oxygen transmission rate of 40-bilayer films deposited on PET as a function of PEI pH. As seen with the previously discussed properties of these films, OTR is highly tailorable using pH of the PEI deposition solution. This trend of decreasing OTR (i.e., increasing oxygen barrier) with higher PEI pH is believed to be due to greater spacing between the clay layers. It should be noted that the dipping process used to make these films results in both sides of the PET substrate being coated, so the coating's contribution to the reported OTR should be divided by two for a single 40-bilayer film value. However, oxygen permeability values (see Table 1), which are decoupled from oxygen transmission rates, take into account this double-sided coating and are reported as a single 40-bilayer film.

The brick wall nanostructure of these clay-based assemblies creates an extremely tortuous pathway for the permeant (63). The oxygen molecule permeating through the thin film will diffuse, taking the path of least resistance, often opting for the long channels between clay layers (within the PEI layers) rather than the openings between clay platelets in the thickness (perpendicular) direction. This causes the O_2 molecule to travel perpendicular to the diffusion direction, thus creating a longer path and reducing the transmission rate. The nonlinear increase in barrier as a function of pH (shown in Figure 8) is attributed to the increase in PEI deposition thickness, resulting in a greater spacing between clay layers. This greater clay spacing is important for increased barrier due to its size relative to O_2 molecules. Assuming MMT platelets have a thickness of exactly 1 nm (50), the approximate clay spacing (or average PEI layer thickness) for (PEI_7/MMT) films is approximately 0.2 nm, increasing to 2.4 nm for (PEI_{10}/MMT) films, according to ellipsometric data (see Figure 2). If it is assumed that each clay platelet is roughly disk-shaped and that clay platelets assume their maximum packing density (a reasonable assumption based on surface images shown in Figure 7), the minimum diameter between coplanar MMT platelets is approximately 31 nm. In this case, there must be sufficient space between clay layers to allow for a penetrant to "prefer" these tortuous channels between clay layers. Moreover, oxygen molecules are known to have a kinetic diameter of 0.346 nm (64), so it would seem that they should always prefer the gaps between coplanar platelets over a path between clay layers. However, this consistent preference would suggest that the permeabilities shown in Table 1 should be very similar among all the films. Experimental data show that increasing the film thickness by a factor of less than three decreases the permeability by 540 times. Therefore, a much more difficult pathway must be traversed by the permeant to fully diffuse through the clay-based assembly than a simple "staircase-like" path through the slits created by coplanar platelets.

Cussler modeled flake-filled membranes and derived the mathematical representation of the permeability of such composites as (63):

$$\frac{P_o}{P} = 1 + \mu\alpha^2\left(\frac{\phi^2}{1-\phi}\right) \tag{4}$$

where P is the composite permeability. Also, this representation is most consistent with a composite content in the semidilute regime (65):

$$\begin{aligned} \phi &\ll 1 \\ \alpha\phi &> 1 \end{aligned} \tag{5}$$

To make theoretical predictions using Cussler's model, montmorillonite clay platelets are assumed to have a geometric factor (μ) of 4/9 (42), and PEI is assumed to have a permeability (P_o) similar to cross-linked PDMS (1.55 cc/(m · day · atm)) (66), because of its elastomeric behavior in the film. Therefore, Cussler's model can be used to find a predicted aspect ratio (α) of the clay platelets from composite permeabilites and known volume fractions of clay (ϕ), but the prediction for the (PEI_{10}/MMT)$_{40}$ thin film, as seen in Table 1, is well outside the accepted range of platelet aspect ratios for Cloisite Na^+ (50). Although it accounts for a tortuous pathway in clay-filled polymers in a more conventional way and at lower clay loadings, Cussler's model cannot accurately predict the barrier behavior of LbL nano-

Table 1. Oxygen Transmission Data for 40-Bilayer Assemblies Made with Clay and PEI at Varying pH Levels

			permeability ($\times 10^{-6}$ cc/(m · day · atm))		
40-BL assembly	OTR (cc/(m · day · atm))	film thickness (nm)	film[a]	total	Cussler's α predictions[b]
PEI_7/MMT	8.42	48.02	48.55	1507.36	
PEI_8/MMT	7.64	65.10	9.28	1368.83	543
PEI_9/MMT	4.53	99.68	1.91	811.06	
PEI_{10}/MMT	0.34	134.12	0.09	60.85	7614

[a] Film permeability was decoupled from the total permeability using a previously described method (62). [b] Clay aspect ratio (α) predicted from Cussler's model (63).

Table 2. Oxygen Transmission Data for Layer-by-Layer Assemblies Made with Clay and PEI at pH 10

			permeability ($\times 10^{-6}$ cc/(m · day · atm))	
no. of bilayers	OTR (cc/(m · day · atm))	film thickness (nm)	film[a]	total
10	5.596	28.27	0.914	1001.91
20	3.007	59.62	0.553	538.61
30	1.485	101.90	0.366	266.10
40	0.339	134.12	0.095	60.85
50	0.129	166.87	0.044	23.08
60	0.036	194.31	0.014	6.40
70	<0.005[b]	230.75	<0.002[b]	<0.90[b]

[a] Film permeability was decoupled from the total permeability using a previously described method (62). [b] The low end detection limit for an Ox Tran 2/21 L module is 0.005 cc/(m^2 day).

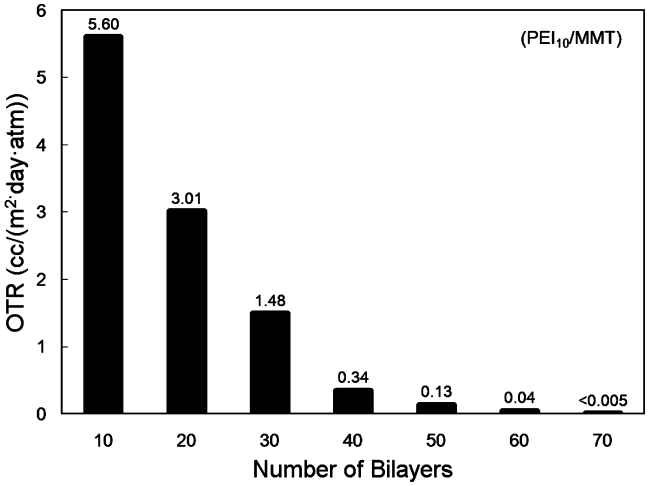

FIGURE 9. Oxygen transmission as a function of number of bilayers of clay and PEI deposited. These films were deposited with pH 10 PEI.

composite films because of their highly oriented, fully aligned, and tightly packed nanostructure. Significantly, these films satisfy eq 5 but have volume fractions greater than 0.5 and an $\alpha\phi$ factor on the order of 100 ($\gg 1$), making them more filler-saturated than this model assumes. Also, geometric models are unable to account for the PEI matrix hydrogen bonding with oxygen via amine moieties to further slow diffusion. In addition, there may also be physiochemical barrier enhancements at the PEI-MMT interfaces, where decreased chain mobility may be forcing the permeant to take an alternate route through the film. In any of these cases, it is clear that thin film barrier enhancements are a result of the increased clay spacing (as seen in Figure 8b), where the thicker $(PEI_{10}/MMT)_{40}$ film reveals a possible foundation for obtaining greater barrier with fewer layers.

Seeing that the $(PEI_{10}/MMT)_{40}$ film had the highest barrier of the 40-bilayer films created, oxygen transmission rate as a function of bilayers deposited was studied for films grown with pH 10 PEI. Figure 9 shows the influence that increasing the number of bilayers has on OTR. When OTR is multiplied by thickness, the 70-bilayer film is shown to exhibit the lowest oxygen permeability ever reported (<0.002 $\times 10^{-6}$ cc/(m · day · atm)) for a polymer composite 231 nm thick (as seen in Table 2). This is also extremely low when compared to a pure SiO_x coating with a permeability of 0.085 $\times 10^{-11}$ cc/(m · day · atm)) (62). These results also show that permeability is not an intrinsic property for these assemblies (i.e., permeability does not directly scale inversely with thickness). Although only increasing the film thickness by a factor of approximately two, the oxygen permeability decreases from 0.366 $\times 10^{-6}$ cc/(m · day · atm) for the 30-bilayer film to less than 0.002 $\times 10^{-6}$ cc/(m · day · atm) for the 70-bilayer film (a decrease in permeability by a factor of more than 180). The decrease in OTR from the 30 to the 70-bilayer film is even more interesting (a difference of approximately 3 orders of magnitude). In general, doubling the thickness of a neat polymer, or a conventionally clay-filled composite, would only result in doubling the barrier performance. However, because the permeating molecule is randomly rerouted perpendicular to its diffusion direction while traveling through these highly oriented assemblies (creating a nonlinear increase in diffusion length), the addition of twice as many clay layers (i.e., PEI/MMT bilayers) exponentially enhances the barrier performance. As seen in Figures 8 and 9, thin film barrier functionality can be tailored based on either the pH of PEI (i.e., barrier increases from low to high pH), or the number of layers deposited (i.e., film thickness).

CONCLUSIONS

Layer-by-layer thin films, made with negatively charged montmorillonite clay platelets and cationic branched polyethylenimine were deposited on a variety of substrates (silicon, Ti/Au crystals, fused quartz, polystyrene, and poly(ethylene terephthalate)) in an effort to examine the influence of pH on growth and properties. Film thickness, based on ellipsometry, QCM, and visible light absorbance, show that these films grow linearly as a function of bilayers deposited, for films made with varying PEI pH. The highest PEI pH studied grows most rapidly because of thicker polymer morphology as compared to lower pH, where higher charge density straightens the polymer through self-repulsion. QCM and visible light absorbance also reveal that these films have extremely high clay loadings (up to 84.3 wt %) yet remain completely transparent (up to 97.5% visible light transmission). TEM and AFM images confirm that the clay platelets orient parallel to the substrate surface when depositing onto the film. At low PEI pH, these films achieve modulus and hardness values as high as 30 and 1 GPa, respectively.

Oxygen permeability is also shown to vary with pH of the PEI deposition solution. At high PEI pH, an oxygen transmission rate below the detection limit of commercial instrumentation (<0.005 cc/(m^2 · day · atm)) is achieved with 70 bilayers. With an exponentially decreasing permeability as thickness is linearly increased, these transparent and flexible thin films may be a useful alternative to SiO_x for food and electronics packaging. Both mechanical and gas barrier properties are attributed to the brick wall nanostructure, formed by highly exfoliated and oriented clay platelets, in these assemblies. These current films are likely to be moisture sensitive (67), but lamination of a moisture barrier would preserve oxygen barrier at high humidity (36). Additionally, PEI can be cross-linked with glutaraldehyde (GA) (68), which has already been shown to enhance mechanical properties (35). Studies are currently underway to examine the influence of cross-linking and greater clay spacing in an attempt to further improve the barrier properties and reduce the number of layers required for super oxygen barrier. Additionally, the permeability of other gases is being measured to determine whether these films are useful for separation. This study lays the foundation for further development of flexible, transparent gas barrier thin films that are needed for a variety of food, biomedical and electronics packaging applications.

Acknowledgment. The authors acknowledge Appleton and Army Natick for financial support of this work. Ms. Charlene Dvoracek is also thanked for TEM imaging assistance and Dr. Woo-Sik Jang for QCM assistance.

Supporting Information Available: X-ray diffraction data for neat MMT powder and thin films deposited on Si (PDF). This material is available free of charge via the Internet at http://pubs.acs.org.

REFERENCES AND NOTES

(1) Ariga, K.; Hill, J. P.; Ji, Q. M. *Phys. Chem. Chem. Phys.* **2007**, *9* (19), 2319–2340.
(2) Bertrand, P.; Jonas, A.; Laschewsky, A.; Legras, R. *Macromol. Rapid Commun.* **2000**, *21* (7), 319–348.
(3) Hammond, P. T. *Adv. Mater.* **2004**, *16* (15), 1271–1293.
(4) Choi, K.; Zentel, R. *Macromol. Chem. Phys.* **2006**, *207* (20), 1870–1879.
(5) Lutkenhaus, J. L.; Hammond, P. T. *Soft Matter* **2007**, *3* (7), 804–816.
(6) Walton, M. D.; Kim, Y. S.; Jan, C. J.; McConnel, E. P.; Everett, W. N.; Grunlan, J. C. *Synth. Met.* **2007**, *157* (16−17), 632–639.
(7) Shim, B. S.; Tang, Z. Y.; Morabito, M. P.; Agarwal, A.; Hong, H. P.; Kotov, N. A. *Chem. Mater.* **2007**, *19* (23), 5467–5474.
(8) Wu, B. Y.; Hou, S. H.; Yin, F.; Li, J.; Zhao, Z. X.; Huang, J. D.; Chen, Q. *Biosens. Bioelectron.* **2007**, *22* (6), 838–844.
(9) Shen, L.; Hu, N. F. *Biomacromolecules* **2005**, *6* (3), 1475–1483.
(10) Yan, X. B.; Chen, X. J.; Tay, B. K.; Khor, K. A. *Electrochem. Commun.* **2007**, *9* (6), 1269–1275.
(11) Zhai, L.; Berg, M. C.; Cebeci, F. C.; Kim, Y.; Milwid, J. M.; Rubner, M. F.; Cohen, R. E. *Nano Lett.* **2006**, *6* (6), 1213–1217.
(12) Bravo, J.; Zhai, L.; Wu, Z. Z.; Cohen, R. E.; Rubner, M. F. *Langmuir* **2007**, *23* (13), 7293–7298.
(13) Ji, J.; Fu, J. H.; Shen, J. C. *Adv. Mater.* **2006**, *18* (11), 1441-+.
(14) Dubas, S. T.; Kumlangdudsana, P.; Potiyaraj, P. *Colloids Surf., A* **2006**, *289* (1−3), 105–109.
(15) Grunlan, J. C.; Choi, J. K.; Lin, A. *Biomacromolecules* **2005**, *6* (2), 1149–1153.
(16) Dvoracek, C. M.; Sukhonosova, G.; Grunlan, J. C. *Langmuir* **2009**, *25* (17), 10322–10328.
(17) De Geest, B. G.; De Koker, S.; Immesoete, K.; Demeester, J.; De Smedt, S. C.; Hennink, W. E. *Adv. Mater.* **2008**, *20* (19), 3687-+.
(18) Macdonald, M.; Rodriguez, N. M.; Smith, R.; Hammond, P. T. *J. Controlled Release* **2008**, *131* (3), 228–234.
(19) Erel-Unal, I.; Sukhishvili, S. A. *Macromolecules* **2008**, *41* (22), 8737–8744.
(20) Sui, Z. J.; Salloum, D.; Schlenoff, J. B. *Langmuir* **2003**, *19* (6), 2491–2495.
(21) Zhang, H. Y.; Wang, D.; Wang, Z. Q.; Zhang, X. *Eur. Polym. J.* **2007**, *43* (7), 2784–2791.
(22) Chang, L.; Kong, X. X.; Wang, F.; Wang, L. Y.; Shen, J. C. *Thin Solid Films* **2008**, *516* (8), 2125–2129.
(23) Tan, H. L.; McMurdo, M. J.; Pan, G. Q.; Van Patten, P. G. *Langmuir* **2003**, *19* (22), 9311–9314.
(24) Mendelsohn, J. D.; Barrett, C. J.; Chan, V. V.; Pal, A. J.; Mayes, A. M.; Rubner, M. F. *Langmuir* **2000**, *16* (11), 5017–5023.
(25) Mermut, O.; Barrett, C. J. *J. Phys. Chem. B* **2003**, *107* (11), 2525–2530.
(26) McAloney, R. A.; Sinyor, M.; Dudnik, V.; Goh, M. C. *Langmuir* **2001**, *17* (21), 6655–6663.
(27) Nolte, A. J.; Treat, N. D.; Cohen, R. E.; Rubner, M. F. *Macromolecules* **2008**, *41* (15), 5793–5798.
(28) Yang, P.; Li, C. L.; Murase, N. *Langmuir* **2005**, *21* (19), 8913–8917.
(29) Zucolotto, V.; Gattas-Asfura, K. M.; Tumolo, T.; Perinotto, A. C.; Antunes, P. A.; Constantino, C. J. L.; Baptista, M. S.; Leblanc, R. M.; Oliveira, O. N. *Appl. Surf. Sci.* **2005**, *246* (4), 397–402.
(30) Kleinfeld, E. R.; Ferguson, G. S. *Science* **1994**, *265* (5170), 370–373.
(31) Ou, R. Q.; Zhang, J. G.; Deng, Y. L.; Ragauskas, A. J. *J. Appl. Polym. Sci.* **2007**, *105* (4), 1987–1992.
(32) Lutkenhaus, J. L.; Olivetti, E. A.; Verploegen, E. A.; Cord, B. M.; Sadoway, D. R.; Hammond, P. T. *Langmuir* **2007**, *23* (16), 8515–8521.
(33) Li, Y. C.; Schulz, J.; Grunlan, J. C. *ACS Appl. Mater. Interfaces* **2009**, *1* (10), 2338–2347.
(34) Wu, Z. Z.; Walish, J.; Nolte, A.; Zhai, L.; Cohen, R. E.; Rubner, M. F. *Adv. Mater.* **2006**, *18* (20), 2699-+.
(35) Podsiadlo, P.; Kaushik, A. K.; Arruda, E. M.; Waas, A. M.; Shim, B. S.; Xu, J. D.; Nandivada, H.; Pumplin, B. G.; Lahann, J.; Ramamoorthy, A.; Kotov, N. A. *Science* **2007**, *318* (5847), 80–83.
(36) Jang, W. S.; Rawson, I.; Grunlan, J. C. *Thin Solid Films* **2008**, *516* (15), 4819–4825.
(37) Grim, R. E. *Science* **1962**, *135* (3507), 890-&.
(38) Graff, G. L.; Burrows, P. E.; Williford, R. E. ; Praino, R. F. , Barrier Layer Technology for Flexible Displays. In *Flexible Flat Panel*

Displays; Crawford, G. P. , Ed.; John Wiley & Sons: New York, 2005; pp 57−77.
(39) Eichie, F. E.; Okor, R. S.; Groning, R. *J. Appl. Polym. Sci.* **2006**, *99* (3), 725–727.
(40) Grunlan, J. C.; Grigorian, A.; Hamilton, C. B.; Mehrabi, A. R. *J. Appl. Polym. Sci.* **2004**, *93* (3), 1102–1109.
(41) Bieder, A.; Gruniger, A.; von Rohr, P. R. *Surf. Coat. Technol.* **2005**, *200* (1−4), 928–931.
(42) Lewis, J. S.; Weaver, M. S. *IEEE J. Sel. Top. Quantum Electron.* **2004**, *10* (1), 45–57.
(43) Czeremuszkin, G.; Latreche, M.; Wertheimer, M. R.; da Silva Sobrinho, A. S. *Plasmas Polym.* **2001**, *6* (1/2), 107–120.
(44) Erlat, A. G.; Spontak, R. J.; Clarke, R. P.; Robinson, T. C.; Haaland, P. D.; Tropsha, Y.; Harvey, N. G.; Vogler, E. A. *J. Phys. Chem. B* **1999**, *103* (29), 6047–6055.
(45) Leterrier, Y. *Prog. Mater. Sci.* **2003**, *48* (1), 1–55.
(46) Choudalakis, G.; Gotsis, A. D. *Eur. Polym. J.* **2009**, *45* (4), 967–984.
(47) Sanchez-Valdes, S.; Lopez-Quintanilla, M. L.; Ramirez-Vargas, E.; Medellin-Rodriguez, F. J.; Gutierrez-Rodriguez, J. M. *Macromol. Mater. Eng.* **2006**, *291* (2), 128–136.
(48) Osman, M. A.; Mittal, V.; Morbidelli, M.; Suter, U. W. *Macromolecules* **2004**, *37* (19), 7250–7257.
(49) Annabi-Bergaya, F. *Microporous Mesoporous Mater.* **2008**, *107* (1−2), 141–148.
(50) Ploehn, H. J.; Liu, C. Y. *Ind. Eng. Chem. Res.* **2006**, *45* (21), 7025–7034.
(51) Owens, D. K. *J. Appl. Polym. Sci.* **1975**, *19* (1), 265–271.
(52) Zhang, D.; Sun, Q.; Wadsworth, L. C. *Polym. Eng. Sci.* **1998**, *38* (6), 965–970.
(53) Geddes, N. J.; Paschinger, E. M.; Furlong, D. N.; Caruso, F.; Hoffmann, C. L.; Rabolt, J. F. *Thin Solid Films* **1995**, *260* (2), 192–199.
(54) Jang, W. S.; Grunlan, J. C. *Rev. Sci. Instrum.* **2005**, *76* (10), 103904.
(55) *ASTM D3985-05 Standard Test Method for Oxygen Gas Transmission Rate Through Plastic Film and Sheeting Using a Coulometric Sensor*; ASTM International: West Conshohocken, PA, 2005.
(56) Suh, J.; Paik, H. J.; Hwang, B. K. *Bioorg. Chem.* **1994**, *22* (3), 318–327.
(57) Podsiadlo, P.; Michel, M.; Lee, J.; Verploegen, E.; Kam, N. W. S.; Ball, V.; Lee, J.; Qi, Y.; Hart, A. J.; Hammond, P. T.; Kotov, N. A. *Nano Lett.* **2008**, *8* (6), 1762–1770.
(58) Pharr, G. M.; Oliver, W. C.; Brotzen, F. R. *J. Mater. Res.* **1992**, *7* (3), 613–617.
(59) Rosidian, A.; Liu, Y. J.; Claus, R. O. *Adv. Mater.* **1998**, *10* (14), 1087-+.
(60) Alexandre, M.; Dubois, P. *Mater. Sci. Eng., R* **2000**, *28* (1−2), 1–63.
(61) Triantafyllidis, K. S.; LeBaron, P. C.; Park, I.; Pinnavaia, T. J. *Chem. Mater.* **2006**, *18* (18), 4393–4398.
(62) Roberts, A. P.; Henry, B. M.; Sutton, A. P.; Grovenor, C. R. M.; Briggs, G. A. D.; Miyamoto, T.; Kano, A.; Tsukahara, Y.; Yanaka, M. *J. Membr. Sci.* **2002**, *208* (1−2), 75–88.
(63) Cussler, E. L.; Hughes, S. E.; Ward, W. J.; Aris, R. *J. Membr. Sci.* **1988**, *38* (2), 161–174.
(64) Park, H. B.; Lee, Y. M. Polymeric Membrane Materials and Potential Use in Gas Separation. In *Advanced Membrane Technology and Applications*; Li, N. N., Fane, A. G., Ho, W. S. W., Matsuura, T., Eds.; John Wiley & Sons.: Hoboken, NJ, 2008; pp 633−669.
(65) DeRocher, J. P.; Gettelfinger, B. T.; Wang, J. S.; Nuxoll, E. E.; Cussler, E. L. *J. Membr. Sci.* **2005**, *254* (1−2), 21–30.
(66) LeBaron, P. C.; Pinnavaia, T. J. *Chem. Mater.* **2001**, *13* (10), 3760–3765.
(67) Yu, H. H.; Cao, T.; Zhou, L. D.; Gu, E. D.; Yu, D. S.; Jiang, D. S. *Sens. Actuators, B* **2006**, *119* (2), 512–515.
(68) Tong, W. J.; Gao, C. Y.; Mohwald, H. *Macromolecules* **2006**, *39* (1), 335–340.

AM900820K